

Phase-field study of size-dependent morphology of austenite–twinned martensite interface in CuAlNi[☆]

K. Tuma^a, S. Stupkiewicz^{a,*}

^a*Institute of Fundamental Technological Research (IPPT), Polish Academy of Sciences,
Pawińskiego 5B, 02-106 Warsaw, Poland.*

Abstract

Size-dependent microstructure of the interface layer between austenite and twinned martensite is studied using a recently developed finite-strain phase-field model. The microstructure is assumed periodic and two-dimensional, however, non-zero out-of-plane displacements are allowed so that the basic microstructural features, specifically the nominal orientation of the twinning and habit planes and the twin fraction, are consistent with the crystallographic theory of martensite. The phase-field computations are carried out for the CuAlNi shape memory alloy undergoing the cubic-to-orthorhombic transformation, and the corresponding four crystallographically distinct microstructures of the austenite–twinned martensite interface are studied in detail. The focus is on size-dependent morphology of the interface layer and on size-dependent interfacial and elastic micro-strain energy contributions. Two mechanisms of reducing the elastic micro-strain energy are revealed: formation of a non-planar zigzag-like interface and twin branching.

Keywords: Microstructure, Phase transformation, Martensite, Phase-field method, Size effects

1. Introduction

Martensitic phase transformations in shape memory alloys (SMA) attract a significant research activity because of the extraordinary behavior of those materials which exhibit the shape memory effect, pseudoelasticity, and related effects (e.g., Otsuka and Wayman, 1998; Bhattacharya, 2003). Transformation between the parent phase (austenite) and the product phase (martensite) is accompanied by formation and evolution of microstructure, and it is of primary interest to understand the corresponding mechanisms. Here, interfaces play a crucial role because evolution of microstructure proceeds by propagation of individual phase boundaries. In this work, using the phase-field method, we study size-dependent morphology of the interface between austenite and twinned martensite and also the related size-dependent elastic micro-strain and interfacial energy contributions.

[☆]Published in *Int J Solids Struct*, Vol.97–98, pp.89–100, 2016, doi: 10.1016/j.ijsolstr.2016.07.040

*Corresponding author. Tel.: (+48) 22 826 12 81 ext. 338.

Email addresses: ktuma@ippt.pan.pl (K. Tuma), sstupkie@ippt.pan.pl (S. Stupkiewicz)

Owing to the transformation strain resulting from the change of crystalline lattice, a single variant of martensite is usually not compatible with the austenite, however, compatibility can be achieved if martensite is internally twinned. The classical crystallographic theory of martensite (Ball and James, 1987; Bhattacharya, 2003) predicts that the interface between austenite and twinned martensite is planar at the macroscale, however, it gives no indication of the morphology of the transition layer at the microscale.

Local incompatibility in the microstructure (e.g., at the austenite–twinned martensite interface) is accommodated by elastic strains, and the corresponding elastic strain energy decreases with decreasing characteristic dimensions of microstructure (e.g., twin spacing). Minimization of elastic strain energy would thus promote infinitely fine microstructures. On the other hand, refinement of microstructure is associated with increasing density of interfaces (e.g., twin boundaries). Since each interface carries some energy, the related total energy would grow to infinity for an infinitely fine microstructure. The actual dimensions of microstructure result thus from an interplay between the two sources of energy, and energy minimization is a natural framework for the analysis of the related effects, provided the total energy, that includes the interfacial energy contributions, is considered. Evolution of microstructure, including formation and annihilation of interfaces, is necessarily accompanied by dissipation, and hence the incremental energy minimization approach is the adequate modeling framework for such problems (Petryk and Stupkiewicz, 2010; Petryk et al., 2010).

This work is concerned with the austenite–twinned martensite interfaces, and the CuAlNi shape memory alloy is taken as an example. Numerous experimental observations confirm that the interface is planar at the macroscale (e.g., Chu and James, 1995; Sun et al., 1999; Seiner et al., 2008), in agreement with the crystallographic theory. Orientation of the interface and twin fraction are also correctly predicted by the crystallographic theory; several comparisons to experiments are given by Bhattacharya (2003). However, very little is known about the morphology of the interface at the microscale in SMA, in general, and in CuAlNi studied in this work, in particular.

As an exception, detailed micrographs of the austenite–martensite interface in CuAlNi have been reported by Ostapovets et al. (2012), see also Zárubová et al. (2010) for the details of the in-situ technique employed. Figure 1 shows the transmission electron microscope (TEM) micrograph reproduced from Ostapovets et al. (2012), in which it is clearly seen that a kind of zigzag interface is formed between austenite and two twin-related variants of martensite (denoted by V1 and V3 in the figure). However, it should be emphasized that microstructural features, such as the twin fraction and the overall orientation of the austenite–martensite interface, are possibly influenced by the experimental conditions (very thin TEM foil of the thickness of 260 nm, stress-induced transformation, non-uniform overall stress state) and hence do not necessarily agree with the predictions of the crystallographic theory.

Other available experimental observations of the direct austenite–martensite interface can be found in Bhattacharya (2003) and Liu and Dunne (2003) (CuAlNi alloy, atomic force microscope (AFM) imaging), and in Hýtch et al. (1999) (CuZnAl alloy, high resolution electron microscopy (HREM)). However, those images are not sufficiently detailed to allow drawing

At a higher scale, a microstructural feature called twin branching is observed experimentally (e.g., Bhattacharya, 2003; Liu and Dunne, 2003; Seiner et al., 2008) and also explained

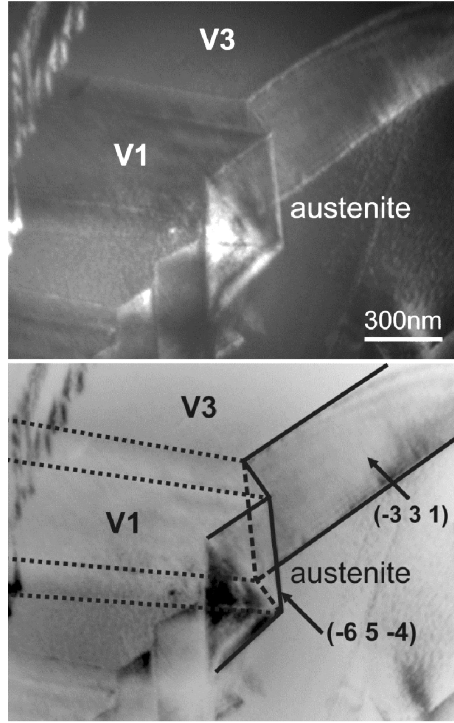


Figure 1: TEM micrograph of the interface between β_1 austenite and twinned γ'_1 martensite: (a) dark field image, reflection 202_{β_1} ; (b) scheme of the interface indicated on the negative image of (a). The zigzag-like interface is composed of planar segments of orientations $(\bar{3}31)_{\beta_1}$ and $(\bar{6}5\bar{4})_{\beta_1}$. Reproduced from Ostapovets et al. (2012) with permission from *Acta Physica Polonica A*.

theoretically (Kohn and Otto, 1997). Specifically, refinement of microstructure (twin spacing) towards the austenite–martensite interface is observed. Again, this can be explained by minimization of energy. Tip-splitting at martensite–martensite interfaces is another mechanism related to branching. It has been observed in experiments (Abeyaratne et al., 1996; Schryvers et al., 2001) and also predicted theoretically (Li and Luskin, 1999; Finel et al., 2010).

Morphology of the transition layer at the austenite–twinned martensite interface in CuAlNi alloy has been studied using a sharp-interface approach by Maciejewski et al. (2005) and Stupkiewicz et al. (2007), and a related study for NiTi alloy has been done by Stupkiewicz et al. (2012). The approach is based on minimization of the elastic strain energy with respect to shape parameters that describe the austenite–martensite interface at the microscale. The analysis delivers also estimates of the energy of elastic micro-strains in the transition layer. This energy, when related to the nominal area of the austenite–martensite interface, is interpreted as a size-dependent (proportional to twin spacing) interfacial energy. While the sharp-interface approach mentioned above relies on minimization of elastic strain energy alone, the effect of atomic-scale interfacial energy of austenite–martensite boundaries has been additionally included in the analysis for zigzag-shaped interfaces (Maciejewski et al., 2005) and for saw-tooth morphology (Stupkiewicz et al., 2012).

In this work, the phase-field method is employed to study the austenite–twinned martensite interface in CuAlNi alloy. Unlike in the earlier sharp-interface approach, in which a specific

class of interface shapes is assumed (Maciejewski et al., 2005; Stupkiewicz et al., 2007, 2012), in the phase-field method the microstructure is obtained as a solution of a boundary value problem. Furthermore, the interfacial energy is naturally included in the phase-field method, and thus the related size effects can be studied directly.

The principle of the phase-field method is that interfaces (here phase boundaries) are modeled as diffuse interfaces. Individual phases are recognized by the so-called order parameter which is continuous in the whole domain, and a transition between the values that indicate individual phases is recognized as a diffuse interface. The literature on the phase-field method is very extensive, and a detailed overview is not attempted here, see Steinbach (2009), Wang and Li (2010) and Mamivand et al. (2013) for recent overviews. Phase-field models that include finite-deformation effects are much more seldom and include Finel et al. (2010), Levitas et al. (2009), Hildebrand and Miehe (2012), Clayton and Knap (2011), and Tůma et al. (2016), see also Mosler et al. (2014) for a homogenization-based formulation employing a partial rank-one convexification of free energy. The model developed by Tůma et al. (2016) has been used in this work.

The paper is organized as follows. In the next section, the classical crystallographic theory of martensite is recalled. The phase-field model and its numerical implementation are summarized in Section 3. In Section 4, the generalized plane strain problem is introduced, and the periodic unit cell that is used in the computations is defined. Finally, in Section 5, results of phase-field simulations of the austenite–twinned martensite interface in CuAlNi alloy are reported, and the obtained size-dependent microstructures are discussed.

2. Crystallographic theory

In most of the known SMA, a single variant of martensite does not form a compatible (stress-free) interface with austenite. However, twinned martensite, i.e., a fine laminate of two twin-related martensite variants, may form a macroscopically compatible interface. The corresponding microstructures can be predicted by the classical crystallographic theory of martensite (Ball and James, 1987; Bhattacharya, 2003). Specifically, conditions of kinematic compatibility between unstressed, but possibly rotated, phases are formulated in the form of the twinning equation,

$$\mathbf{R}\mathbf{U}_I - \mathbf{U}_J = \mathbf{a} \otimes \mathbf{l}, \quad (1)$$

and the habit plane equation,

$$\hat{\mathbf{R}}(\hat{\eta}\mathbf{R}\mathbf{U}_I + (1 - \hat{\eta})\mathbf{U}_J) - \mathbf{I} = \mathbf{b} \otimes \mathbf{m}. \quad (2)$$

The twinning equation (1) expresses kinematic compatibility between two variants of martensite with the transformation stretches (Bain strains) \mathbf{U}_I and \mathbf{U}_J , and the habit plane equation (2) expresses the kinematic compatibility between undeformed austenite and twinned martensite, the latter considered in the average sense. The unknowns are the twinning plane normal \mathbf{l} , the habit plane normal \mathbf{m} , vectors \mathbf{a} and \mathbf{b} , rotations \mathbf{R} and $\hat{\mathbf{R}}$, and the twin fraction $\hat{\eta}$. Solution method can be found in Ball and James (1987) and Bhattacharya (2003), and results corresponding to the CuAlNi alloy, which is studied in this work, are provided in Section 5.1.

For future use, according to (1) and (2), we introduce the deformation gradients of the first martensitic variant \mathbf{F}_I , the other martensitic variant \mathbf{F}_J and austenite \mathbf{F}_a equal to:

$$\mathbf{F}_I = \hat{\mathbf{R}}\mathbf{R}\mathbf{U}_I, \quad \mathbf{F}_J = \hat{\mathbf{R}}\mathbf{U}_J, \quad \mathbf{F}_a = \mathbf{I}, \quad (3)$$

all corresponding to the stress-free state with zero elastic strain energy.

3. Finite-strain phase-field model for austenite and two variants of martensite

In this section, we briefly present the finite-strain phase-field model for austenite and two variants of martensite that has been developed recently by Tůma et al. (2016). Fundamentals of the phase-field method can be found in Penrose and Fife (1990), Wang and Khachaturyan (1997), Chen (2002), and Steinbach (2009), and recent developments concerning finite-strain models in Levitas et al. (2009), Clayton and Knap (2011), and Hildebrand and Miehe (2012). For the details of the present model, the reader is referred to Tůma et al. (2016).

As it is typical for the phase-field approach, a diffuse-interface approximation is introduced for the interfaces that separate the individual phases during phase transformation. For that purpose, so-called order parameters are introduced which vary smoothly between the values that indicate the pure phases, while intermediate values correspond to diffuse interfaces. In the present model, two hierarchical order parameters η and η_0 are employed: η_0 is the volume fraction of austenite and η the *relative* volume fraction of the first variant of martensite. The volume fractions of the two martensite variants are thus equal to $(1 - \eta_0)\eta$ and $(1 - \eta_0)(1 - \eta)$. All volume fractions refer to the reference configuration. Clearly, both order parameters have to satisfy the inequality constraints

$$0 \leq \eta, \eta_0 \leq 1. \quad (4)$$

The deformation of the body is defined by the mapping $\mathbf{x} = \boldsymbol{\varphi}(\mathbf{X})$ given on the reference domain B that corresponds to undeformed austenite, and $\mathbf{u} = \mathbf{x} - \mathbf{X}$ is the corresponding displacement field. The deformation gradient $\mathbf{F} = \nabla\boldsymbol{\varphi} = \mathbf{I} + \nabla\mathbf{u}$ is multiplicatively decomposed into the elastic part \mathbf{F}_e and transformation part \mathbf{F}_t , such that

$$\mathbf{F} = \mathbf{F}_e\mathbf{F}_t. \quad (5)$$

The transformation part \mathbf{F}_t is defined by the following logarithmic mixing rule (Tůma et al., 2016),

$$\mathbf{F}_t = \exp\left((1 - \eta_0)(\eta \log \mathbf{U}_I + (1 - \eta) \log \mathbf{U}_J)\right), \quad (6)$$

in which the logarithmic transformation strain of the phase mixture is obtained by averaging the logarithmic transformation strains of the individual phases. Clearly, we have $\mathbf{F}_t = \mathbf{I}$ for pure austenite ($\eta_0 = 1$) and $\mathbf{F}_t = \mathbf{U}_I$ or $\mathbf{F}_t = \mathbf{U}_J$ for pure martensite variants ($\eta_0 = 0$ and $\eta = 0$ or 1).

The logarithmic mixing rule (6) ensures that volume changes are treated consistently. In particular, for fixed η_0 the determinant of \mathbf{F}_t does not change with varying η which means that the change from one variant of martensite to the other variant of martensite is isochoric. This does not hold for linear mixing of strain measures other than the logarithmic one.

The total free energy density F comprises the bulk part F_B and the interfacial part F_Γ , i.e. $F = F_B + F_\Gamma$. The bulk free energy F_B describes the anisotropic elasticity by

$$F_B = (1 - \eta_0)F_m^0 + \frac{1}{2}(\det \mathbf{F}_t)\mathbf{E}_e \cdot \mathbf{L}\mathbf{E}_e, \quad (7)$$

where F_m^0 is the chemical free energy of the martensite (taking unstressed austenite as a reference, i.e. $F_a^0 = 0$), \mathbf{E}_e is the elastic Green strain, $\mathbf{E}_e = \frac{1}{2}(\mathbf{F}_e\mathbf{F}_e^T - \mathbf{I})$, and \mathbf{L} is the average anisotropic elastic stiffness tensor

$$\mathbf{L} = \eta_0\mathbf{L}_a + (1 - \eta_0)(\eta\mathbf{L}_I + (1 - \eta)\mathbf{L}_J). \quad (8)$$

Here, \mathbf{L}_a is the elastic stiffness tensor of the austenite and \mathbf{L}_I is that of the variant I . Note that \mathbf{L}_I and \mathbf{L}_J correspond to the intermediate configuration specified by $\mathbf{F}_t = \mathbf{U}_I$ and $\mathbf{F}_t = \mathbf{U}_J$, respectively, hence the factor $(\det \mathbf{F}_t)$ in (7).

The interfacial part of the free energy is divided into the energy F_Γ^{am} of austenite–martensite interfaces and energy F_Γ^{tw} of martensite–martensite interfaces, i.e. $F_\Gamma = F_\Gamma^{\text{am}} + F_\Gamma^{\text{tw}}$, where

$$F_\Gamma^{\text{am}} = \gamma_{\text{am}} \left(\frac{4\ell}{\pi} |\nabla \eta_0|^2 + \frac{4}{\pi\ell} \eta_0(1 - \eta_0) \right), \quad (9)$$

$$F_\Gamma^{\text{tw}} = \gamma_{\text{tw}} \left(\frac{4\ell}{\pi} |\nabla \eta|^2 + (1 - \eta_0) \frac{4}{\pi\ell} \eta(1 - \eta) \right). \quad (10)$$

Here, F_Γ^{am} is specified by the standard double-obstacle potential (Steinbach, 2009) in which γ_{am} denotes the interfacial energy density per unit area of the interface and ℓ is the interface thickness parameter. In accord with the concept of hierarchical order parameters, the energy F_Γ^{tw} of twin boundaries is defined analogously, except that the second term is scaled by the factor $(1 - \eta_0)$, see Tůma et al. (2016) for the corresponding discussion, and γ_{tw} denotes the twin boundary energy. A possible dependence of the interfacial energy on the interface orientation is not included in the present model. Note that in the present work, we have adopted the double-obstacle potential which results in less diffuse interfaces as compared to the double-well potential used by Tůma et al. (2016).

Finally, a quadratic dissipation potential D is defined as

$$D = \frac{1}{2L_0} \dot{\eta}_0^2 + \frac{1}{2L} (1 - \eta_0) \dot{\eta}^2, \quad (11)$$

where L and L_0 denote the mobility parameters. Again, the factor of $(1 - \eta_0)$ is introduced to scale the dissipation associated with the evolution of the relative volume fraction η of martensite so that the second term vanishes in the austenite (for $\eta_0 = 1$).

The following global rate-potential Π can now be defined

$$\Pi[\dot{\mathbf{u}}, \dot{\eta}, \dot{\eta}_0; \mathbf{u}, \eta, \eta_0] = \int_B (\dot{F} + D) \, d\mathbf{X} + \dot{\Omega}, \quad (12)$$

where Ω denotes the potential of external loads, and the evolution problem is formulated as minimization of Π with respect to the rates $\dot{\mathbf{u}}, \dot{\eta}$ and $\dot{\eta}_0$ under the constraints (4), viz.

$$\forall t > t_0 \text{ find } \min_{\dot{\mathbf{u}}, \dot{\eta}, \dot{\eta}_0} \Pi[\dot{\mathbf{u}}, \dot{\eta}, \dot{\eta}_0; \mathbf{u}, \eta, \eta_0] \text{ subject to } 0 \leq \eta, \eta_0 \leq 1. \quad (13)$$

With reference to the numerical implementation of the model, the minimization problem (13) is discretized in time using the backward Euler method. The solution known from the previous time step t_n is denoted by $(\mathbf{u}_n, \eta_n, \eta_{0,n})$, while the subscript for the unknowns at the current time t_{n+1} is omitted for brevity, thus $(\mathbf{u}, \eta, \eta_0) = (\mathbf{u}_{n+1}, \eta_{n+1}, \eta_{0,n+1})$. Upon time integration, the following incremental potential Π_τ is obtained,

$$\Pi_\tau[\mathbf{u}, \eta, \eta_0; \hat{\eta}_0] = \int_B (F(\nabla \mathbf{u}, \eta, \eta_0, \nabla \eta, \nabla \eta_0) + D_\tau(\eta, \eta_0, \hat{\eta}_0)) \, d\mathbf{X}, \quad (14)$$

where the incremental dissipation potential D_τ is defined as

$$D_\tau(\eta, \eta_0, \hat{\eta}_0) = \frac{\tau}{2L_0} \left(\frac{\eta_0 - \eta_{0,n}}{\tau} \right)^2 + \frac{\tau}{2L} (1 - \hat{\eta}_0) \left(\frac{\eta - \eta_n}{\tau} \right)^2, \quad (15)$$

and $\Omega = 0$ is assumed. Here, $\tau = t_{n+1} - t_n$ denotes the time increment, and $\hat{\eta}_0$ has been introduced as an additional variable in order to indicate the state-dependence of the dissipation potential. The incremental problem is now formulated as follows

$$\text{find } \min_{\mathbf{u}, \eta, \eta_0} \Pi_\tau[\mathbf{u}, \eta, \eta_0; \hat{\eta}_0] \Big|_{\hat{\eta}_0 = \eta_0} \quad \text{subject to } 0 \leq \eta, \eta_0 \leq 1. \quad (16)$$

Note that minimization is here performed with respect to $(\mathbf{u}, \eta, \eta_0)$ but not with respect to $\hat{\eta}_0 = \eta_0$ so that the incremental problem (16) is not a genuine minimization problem, a more detailed discussion can be found in Tůma et al. (2016).

In the computational scheme, the inequality constraints $0 \leq \eta_0 \leq 1$ and $0 \leq \eta \leq 1$ are efficiently enforced using the augmented Lagrangian method (Bertsekas, 1996; Stupkiewicz and Petryk, 2013). Compared to Tůma et al. (2016), the computational scheme has been improved by introducing a single variable that represents either the primal variable (here the order parameter) or the corresponding Lagrange multiplier. The treatment is similar to that described in Appendix C in Lengiewicz et al. (2014) (the details are omitted here) and results in a reduction of the number of global unknowns and the related reduction of the computational cost.

The model has been implemented in the finite element method, and the *AceGen/AceFEM* system (Korelc, 2002, 2009) has been used for that purpose. The system of nonlinear equations resulting from the finite element discretization is solved simultaneously with respect to all unknowns using the (semi-smooth) Newton method. The automatic differentiation (AD) technique that is available in *AceGen* has been applied to derive the exact tangent matrix corresponding to the present monolithic scheme, and the exact linearization is highly beneficial for the overall efficiency of the scheme. Application of the logarithmic mixing rule (6) involves computation of the matrix exponential as well as its first and second derivatives. This has been efficiently implemented using the closed-form representation of matrix exponential developed by Korelc and Stupkiewicz (2014) and Hudobivnik and Korelc (2016).

As explained in the next section, a generalized plane-strain problem is considered in this work. In the computations, a four-node quadrilateral element with bilinear shape functions has been used with three components of displacement \mathbf{u} and two scalar variables corresponding to η_0 and η per node. In order to avoid spurious stresses due to incompatible approximation of \mathbf{F} and \mathbf{F}_t , \mathbf{F}_t is assumed to be constant over the element with the value corresponding to η_0 and η evaluated at the center of the element, see Tůma et al. (2016) for details.

4. Generalized plane-strain problem

The aim of this work is to apply the phase-field method to study in detail the microstructure and energy of austenite–twinned martensite interfaces. Following the earlier sharp-interface studies (Maciejewski et al., 2005; Stupkiewicz et al., 2007), the microstructure is assumed periodic and two-dimensional, as illustrated in Fig. 2. The latter assumption implies that all the fields (displacements, order parameters, stresses, strains, etc.) do not depend on the coordinate orthogonal to the plane parallel to the twin plane normal \mathbf{l} and habit plane normal \mathbf{m} predicted by the crystallographic theory, see Section 2. This defines a special two-dimensional generalized plane-strain problem. Note, however, that even though the problem is two-dimensional the component of the displacement field orthogonal to the plane of analysis is not equal to zero, and thus stress and strain tensors are fully three-dimensional.

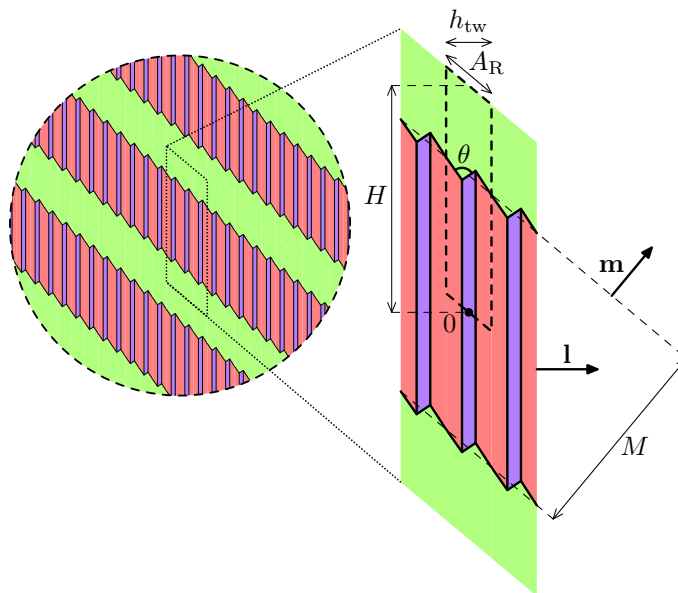


Figure 2: Periodic microstructure and the unit cell used for the analysis of the austenite–twinned martensite interface (shown in reference configuration). Green, red and blue indicate, respectively, the domains occupied by the austenite and the two variants of martensite. The dashed line indicates the computational cell B_C that constitutes one half of the periodic unit cell B , see text.

The microstructure is controlled by prescribing the average deformation gradient to be equal to $\bar{\mathbf{F}}$, i.e.

$$\langle \mathbf{F} \rangle = \bar{\mathbf{F}}, \quad \langle \cdot \rangle = \frac{1}{|B|} \int_B (\cdot) d\mathbf{X}, \quad (17)$$

where $\langle \cdot \rangle$ denotes the averaging within the periodic unit cell B , and $\bar{\mathbf{F}}$ is constructed by weighting the deformation gradients resulting from the crystallographic theory, cf. Eq. (3), according to

$$\bar{\mathbf{F}} = \bar{\eta}_0 \mathbf{F}_a + (1 - \bar{\eta}_0) (\bar{\eta} \mathbf{F}_I + (1 - \bar{\eta}) \mathbf{F}_J). \quad (18)$$

Here $\bar{\eta}$ and $\bar{\eta}_0$ are control parameters that are expected to be close to the average values, respectively, $\langle \eta \rangle$ and $\langle \eta_0 \rangle$ of order parameters η and η_0 . The condition $\langle \mathbf{F} \rangle = \bar{\mathbf{F}}$ is enforced

by prescribing the following periodic boundary conditions on the displacement \mathbf{u} ,

$$\mathbf{u}(\mathbf{X}) = (\bar{\mathbf{F}} - \mathbf{I})\mathbf{X} + \tilde{\mathbf{u}}(\mathbf{X}) \quad \text{for } \mathbf{X} \in \partial B, \quad \text{where } \tilde{\mathbf{u}} \text{ is } B\text{-periodic}, \quad (19)$$

and by enforcing B -periodicity of order parameters η and η_0 .

The control parameter $\bar{\eta}$ is prescribed as $\bar{\eta} = \hat{\eta}$, where $\hat{\eta}$ is the twin fraction known from the solution of the habit plane equation (2). The control parameter $\bar{\eta}_0$ is adjusted such that the thickness of the layer of austenite is sufficiently large so that the stress fields of the two neighboring interfaces do not interact. In practice, $\bar{\eta}_0$ varies between 0.1 and 0.6 depending on twin spacing h_{tw} , see Appendix A. The control parameters $\bar{\eta}$ and $\bar{\eta}_0$ are fixed during each analysis, and the microstructure is allowed to evolve until a steady-state (equilibrium) microstructure is reached. The results reported below correspond to such steady-state microstructures.

The computational cost can be reduced by observing that, in addition to periodicity, the microstructure exhibits a two-fold symmetry with respect to point 0 shown in Fig. 2. As a result, the computations can be carried out for only one half of the periodic unit cell. The corresponding computational cell B_C is indicated by dashed lines in Fig. 2. Appropriate boundary conditions are enforced by prescribing periodicity of the displacement fluctuation $\tilde{\mathbf{u}}$ along the vertical edges of the computational cell B_C , and by prescribing anti-periodicity of $\tilde{\mathbf{u}}$ along the bottom and top edges of the computational cell. The order parameters are enforced to be periodic along the vertical edges, symmetric with respect to point 0 along the bottom edge with an analogous symmetry condition enforced on the top edge.

The computational study reported below is concerned with size-effects and, in particular, with the effect of twin spacing h_{tw} on microstructure and energy of austenite–twinned martensite interface. Since plate thickness M is an independent parameter that may also influence the results, this parameter is determined according to the procedure described in Appendix A. In particular, by employing a simple model based on minimization of the total interfacial energy, this procedure ensures that only one period of microstructure forms within the computational cell.

5. Phase-field simulations

5.1. CuAlNi shape memory alloy: material parameters

The computations are carried out for a CuAlNi shape memory alloy undergoing the cubic-to-orthorhombic $\beta_1 \rightarrow \gamma'_1$ transformation that involves six variants of martensite. The crystallographic theory predicts 96 austenite–twinned martensite interfaces (Bhattacharya, 2003), but only four of them are crystallographically distinct. They are denoted by M1 to M4, and the corresponding solutions of the twinning equation (1) and the habit plane equation (2) are provided in Table 1. Those microstructures correspond to the variant pair $(I, J) = (1, 3)$ characterized by the following transformation stretch tensors,

$$\mathbf{U}_1 = \begin{pmatrix} \frac{\alpha+\gamma}{2} & 0 & \frac{\alpha-\gamma}{2} \\ 0 & \beta & 0 \\ \frac{\alpha-\gamma}{2} & 0 & \frac{\alpha+\gamma}{2} \end{pmatrix}, \quad \mathbf{U}_3 = \begin{pmatrix} \frac{\alpha+\gamma}{2} & \frac{\alpha-\gamma}{2} & 0 \\ \frac{\alpha-\gamma}{2} & \frac{\alpha+\gamma}{2} & 0 \\ 0 & 0 & \beta \end{pmatrix}, \quad (20)$$

with the stretch parameters $\alpha = 1.0619$, $\beta = 0.9178$ and $\gamma = 1.0230$ (Bhattacharya, 2003).

	Microstructure M1	Microstructure M2
<i>Type I twins</i>		
$\hat{\eta}$	0.2902	0.2902
\mathbf{l}	(0.0, -0.7071, 0.7071)	(0.0, -0.7071, 0.7071)
\mathbf{m}	(0.6350, 0.1908, 0.7486)	(-0.7151, 0.2579, -0.6497)
	Microstructure M3	Microstructure M4
<i>Type II twins</i>		
$\hat{\eta}$	0.3008	0.3008
\mathbf{l}	(0.2282, 0.6884, 0.6884)	(0.2282, 0.6884, 0.6884)
\mathbf{m}	(0.6345, 0.2607, 0.7276)	(0.7304, 0.1430, -0.6679)

Table 1: Microstructure parameters of the austenite–twinned martensite interfaces in the $\beta_1 \rightarrow \gamma'_1$ transformation in CuAlNi alloy for the variant pair $(I, J) = (1, 3)$.

The following material parameters are used in the present phase-field computations. The anisotropic elastic constants of single-crystal austenite and martensite are taken from the literature (Suezawa and Sumino, 1976; Yasunaga et al., 1983). The interfacial energy densities are adopted as $\gamma_{\text{tw}} = 0.02 \text{ J/m}^2$, $\gamma_{\text{am}} = 0.2 \text{ J/m}^2$ (Petryk et al., 2010; Tůma et al., 2016). Finally, the microstructure is analyzed in an equilibrium temperature, and thus the chemical free energy is set to zero, $F_{\text{m}}^0 = F_{\text{a}}^0 = 0$.

In addition to the above material parameters, the phase-field method involves two parameters that define the thickness and mobility of diffuse interfaces. The mobility parameters, assumed equal to $L = L_0 = 100 \text{ (Pas)}^{-1}$, do not affect the steady-state microstructures studied below, as they only define the time scale of the transient microstructure evolution process. On the other hand, the interface thickness parameter ℓ , assumed here identical for austenite–martensite and martensite–martensite (twin) interfaces, does affect the results, in terms of both microstructural features and the overall energy stored in the microstructure, as illustrated by the numerical examples below.

It is noted that the value of ℓ imposes a constraint on the spatial discretization. Specifically, the mesh must be sufficiently fine to properly represent diffuse interfaces, and the ratio of $h/\ell \approx 0.5$ has been adopted in the computations, h denoting the element size. Accordingly, for fixed ℓ and thus for fixed element size h , the number of elements grows with increasing twin spacing h_{tw} . The related increase of computational cost limits the range of twin spacings that can be analyzed for a fixed value of ℓ . Several values of the interface thickness parameter, specifically $\ell = 0.4, 0.8, 1.6$ and 4 nm , have thus been used in the computations so that a wide range of twin spacings could be studied.

For fixed ℓ , the twin spacing h_{tw} is also bounded from below due to the finite thickness of twin boundaries. Note that the theoretical thickness of a stress-free diffuse interface is equal to $\pi\ell$ and that the computational cell accommodates two twin boundaries per one twin spacing.

5.2. Zigzag-like morphology in microstructure M2

Microstructure M2 is discussed first. The obtained morphologies are shown in Fig. 3 for two values of interface thickness $\ell = 0.4$ and 0.8 nm , and for several values of twin spacing h_{tw} . For

each case, the figure presents the distribution of a composite parameter $\eta^* = (1 - \eta_0)(1 - 2\eta)$ in the vicinity of the actual austenite–martensite interface (the computational cell is significantly larger). Austenite is indicated by $\eta^* = 0$ (denoted by green on the color map), and the two variants of martensite are indicated by $\eta^* = \pm 1$ (denoted by blue and red). Intermediate colors indicate diffuse interfaces. Note that the green color appears also within diffuse martensite–martensite interfaces, but there it does not indicate austenite, and this visual effect is a consequence of the adopted color scale. Here and for the other microstructures, the results are reported in the deformed configuration, and the in-plane deformation can be observed in the form of bending of the unit cell (the non-zero out-of-plane displacement is not visualized). This effect is more visible for microstructures M1 and M4. A complete set of simulation results, including the results for $\ell = 1.6$ and 4 nm, is reported in the supplementary material accompanying this paper.

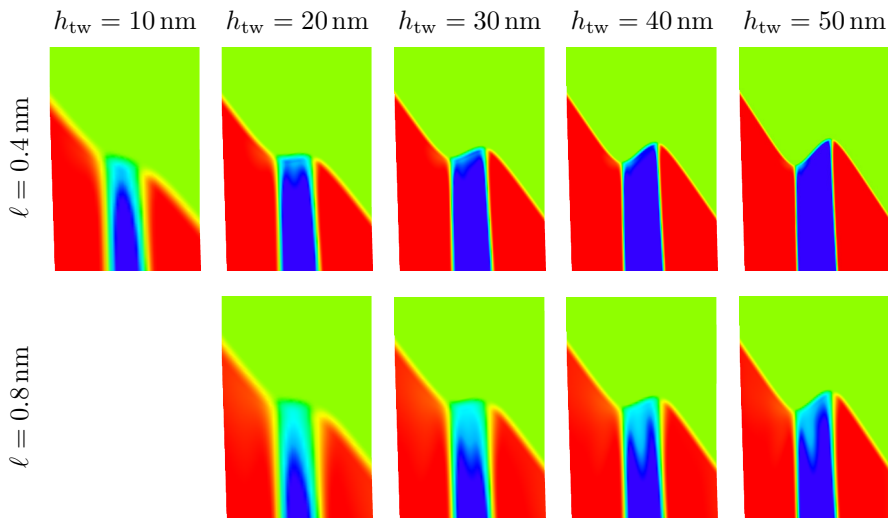


Figure 3: Microstructure M2: dependence of the microstructure on the twin spacing h_{tw} for $\ell = 0.4$ and 0.8 nm. Austenite is indicated by green and the two variants of martensite are indicated by blue and red. Diffuse interfaces are indicated by intermediate colors, see text for details.

It is seen that microstructure M2 exhibits a tendency to form a zigzag-like interface. This is in a very good agreement with the results of the sharp-interface modeling reported by Stupkiewicz et al. (2007), where low-energy morphologies were found using a shape-optimization technique. It can also be observed in Fig. 3 that with decreasing twin spacing h_{tw} , the interface becomes more and more planar. This behavior can be explained by a competition between the interfacial energy of direct austenite–martensite interfaces (characterized by the density γ_{am}) and the energy of elastic micro-strains that accommodate local incompatibility of the phases. The former would be the lowest for a perfectly planar interface, the latter is minimized for a zigzag-shaped interface. For the finest microstructure, i.e. for $h_{tw} = 10$ nm, the interfacial energy prevails and the interface is almost planar. With increasing twin spacing h_{tw} , the total interfacial energy of the austenite–martensite interface (integrated over the computational cell B_C) scales approximately linearly with h_{tw} while the total elastic micro-strain energy scales approximately with the square of h_{tw} , and thus the zigzag morphology becomes energetically

preferable. A more detailed analysis of the different energy contributions is carried out in Section 5.4.

Figure 4 presents the dependence of the zigzag angle θ , see Fig. 2, on h_{tw} and ℓ . The angle θ has been computed by fitting a zigzag line to the isoline of $\eta_0 = 0.5$. Results corresponding to small ℓ show a very good agreement with the prediction of the sharp-interface model (Maciejewski et al., 2005), where a class of zigzag-shaped interfaces of varying angle θ was analyzed.

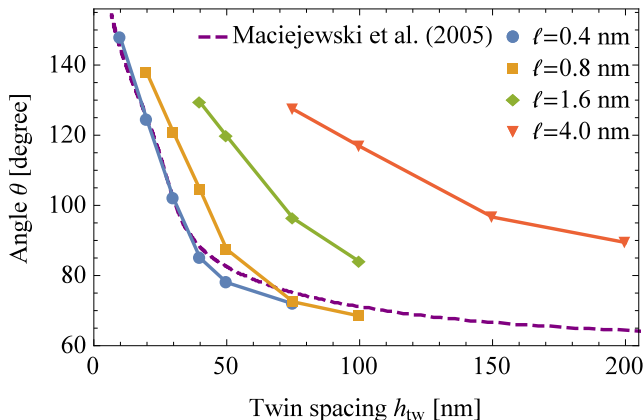


Figure 4: Microstructure M2: dependence of the angle θ , see Fig. 2, on h_{tw} and ℓ . Dashed line indicates prediction of the sharp-interface model of Maciejewski et al. (2005).

The effect of the interface thickness parameter ℓ on the obtained microstructure is two-fold. Firstly, with increasing ℓ , the microstructure becomes more diffuse. Specifically, one may observe relatively large zones in which order parameter η takes values between 0 and 1. The stresses are expected to be high in those zones, and the elastic strain energy (F_B) is locally reduced at the cost of increased interfacial energy (F_{Γ}^{tw}), the latter otherwise being non-zero only within the actual diffuse interfaces. However, the qualitative features of the solution are not visibly affected by the mentioned effect. Secondly, for a fixed twin spacing h_{tw} , the local austenite–martensite interface becomes more planar for increasing ℓ . This can be seen in Figs. 3 and 5 and also, visualized in terms of the zigzag angle θ , in Fig. 4. Both effects are observed also for microstructures M1, M3 and M4 discussed below.

5.3. Tendency to twin branching in microstructures M1, M3 and M4

Microstructures M1, M3 and M4 are discussed together as they exhibit a common feature, namely the tendency to form twin branches. This feature, which is very different from the zigzag pattern observed in microstructure M2, is illustrated for microstructure M3 in Fig. 6. With increasing twin spacing h_{tw} , the microstructure is locally refined by branching, i.e. by forming thin needle-like plates of one martensite variant within the other one. This reduces the effective twin spacing and provides a mechanism for reducing the elastic strain energy. At the same time, additional martensite–martensite interfaces are formed and the interfacial energy increases. Formation of size dependent microstructures is thus a result of a competition between interfacial and bulk (elastic strain) energy contributions. Twin branching is observed for both $\ell = 0.4$ nm and $\ell = 0.8$ nm, though it is somewhat delayed for larger ℓ .

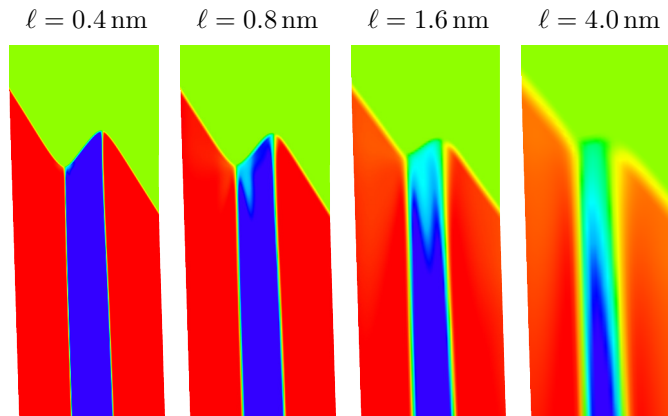


Figure 5: Microstructure M2: dependence of the microstructure on interface thickness ℓ for fixed $h_{tw} = 75$ nm.

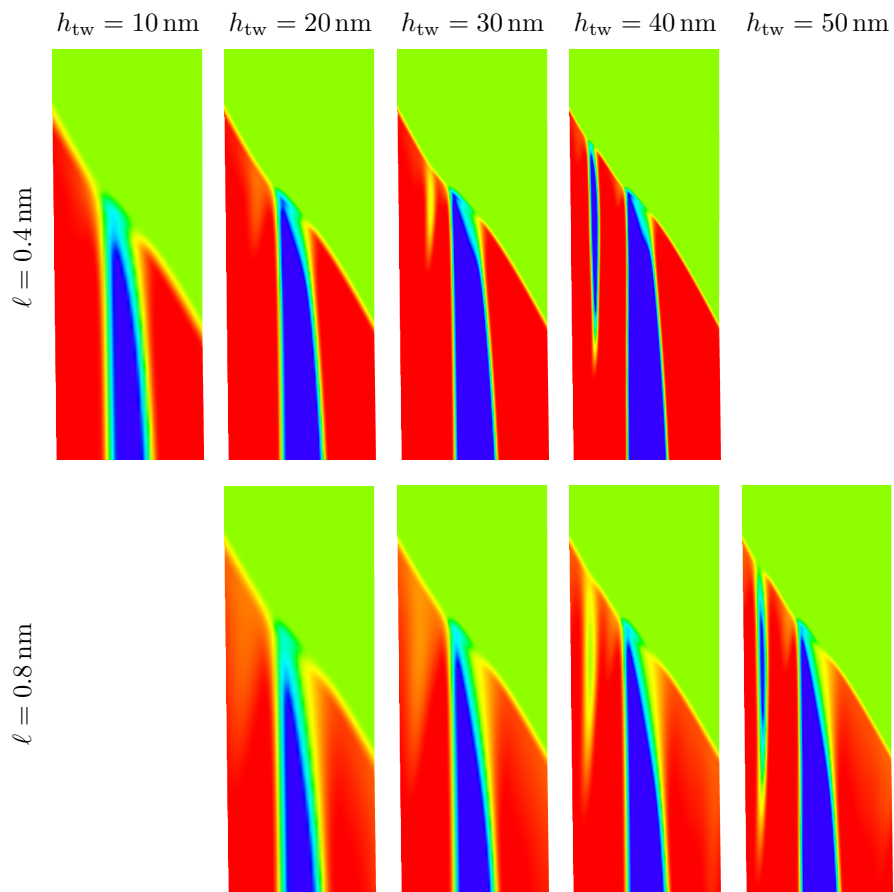


Figure 6: Microstructure M3: dependence on twin spacing h_{tw} for $\ell = 0.4$ and 0.8 nm.

Branching is also observed for microstructures M1 and M4, see Fig. 7. The effect of interface thickness ℓ is similar to that illustrated in Fig. 6, and hence only the results corresponding to $\ell = 0.4$ nm are reported in Fig. 7. It is recalled that a complete set of simulation results is provided in the supplementary material accompanying this paper. For better visualization of the branched microstructures M1 and M4, the periodic microstructures corresponding to $h_{\text{tw}} = 40$ nm have been replicated and the obtained overall view of the austenite–martensite interface is presented in Fig. 8.

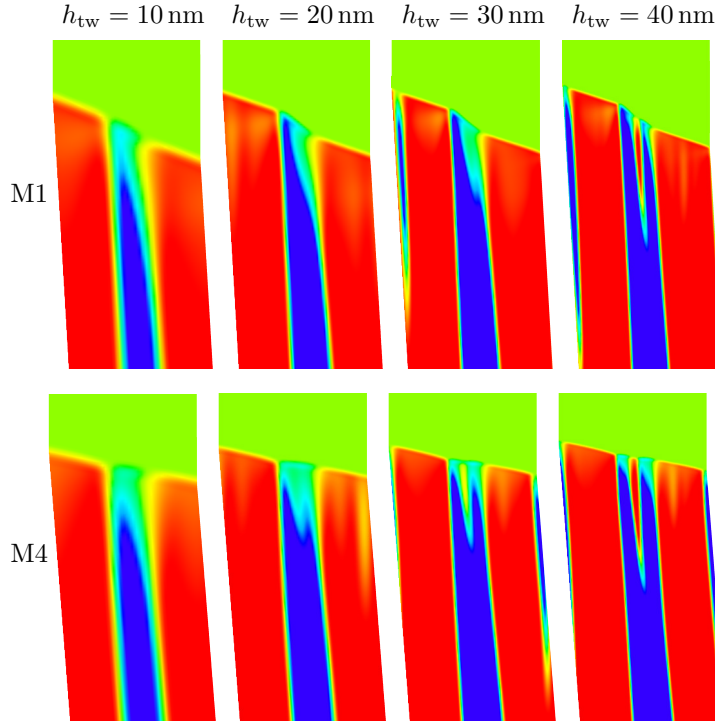


Figure 7: Microstructures M1 (top) and M4 (bottom): dependence on twin spacing h_{tw} for $\ell = 0.4$ nm.

5.4. Size-dependent energy contributions

Although the mechanism of reducing the elastic strain energy is different in microstructure M2 (zigzag-shaped interface) and in microstructures M1, M3 and M4 (twin branching), it turns out that the qualitative dependence of the individual energy contributions is quite similar for all microstructures. To illustrate those dependencies, let us define the overall elastic micro-strain energy density $\bar{\gamma}_{\text{am}}^e$ and the overall interfacial energy density $\bar{\gamma}_{\text{am}}$, both per unit area of the nominal austenite–martensite interface,

$$\bar{\gamma}_{\text{am}}^e = \frac{1}{A_{\text{R}}} \int_{B_{\text{C}}} F_{\text{B}} \, d\mathbf{X}, \quad \bar{\gamma}_{\text{am}} = \frac{1}{A_{\text{R}}} \int_{B_{\text{C}}} F_{\Gamma}^{\text{am}} \, d\mathbf{X}, \quad (21)$$

where A_{R} denotes the nominal area of the austenite–martensite interface, see Fig. 2. Note that the chemical energy is assumed equal to zero, $F_{\text{a}}^0 = F_{\text{m}}^0 = 0$, hence the bulk free energy F_{B} comprises only the elastic strain energy. Dependence of $\bar{\gamma}_{\text{am}}^e$ and $\bar{\gamma}_{\text{am}}$ on twin spacing h_{tw} is depicted in Fig. 9.

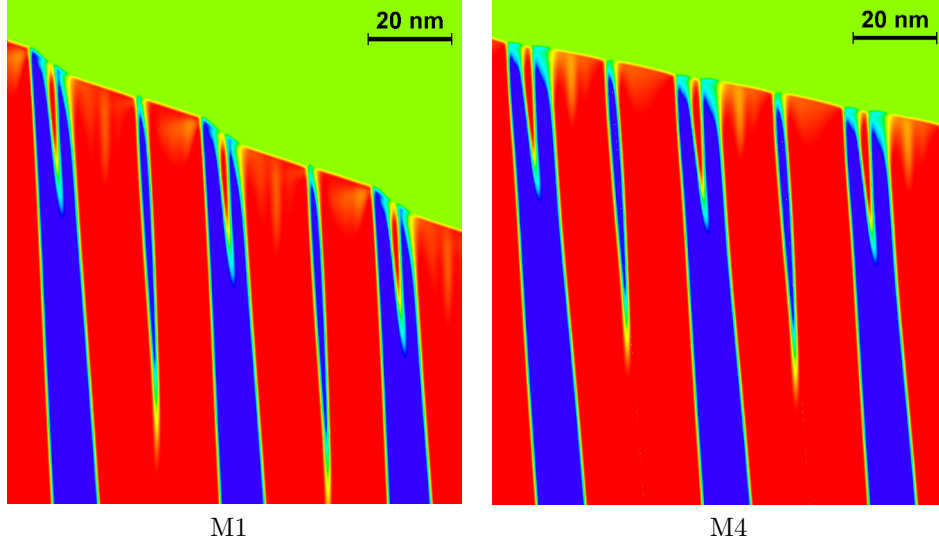


Figure 8: Visualization of twin branching in microstructures M1 and M4 for $h_{tw} = 40$ nm and $\ell = 0.4$ nm (replication of the results obtained for a periodic computational cell).

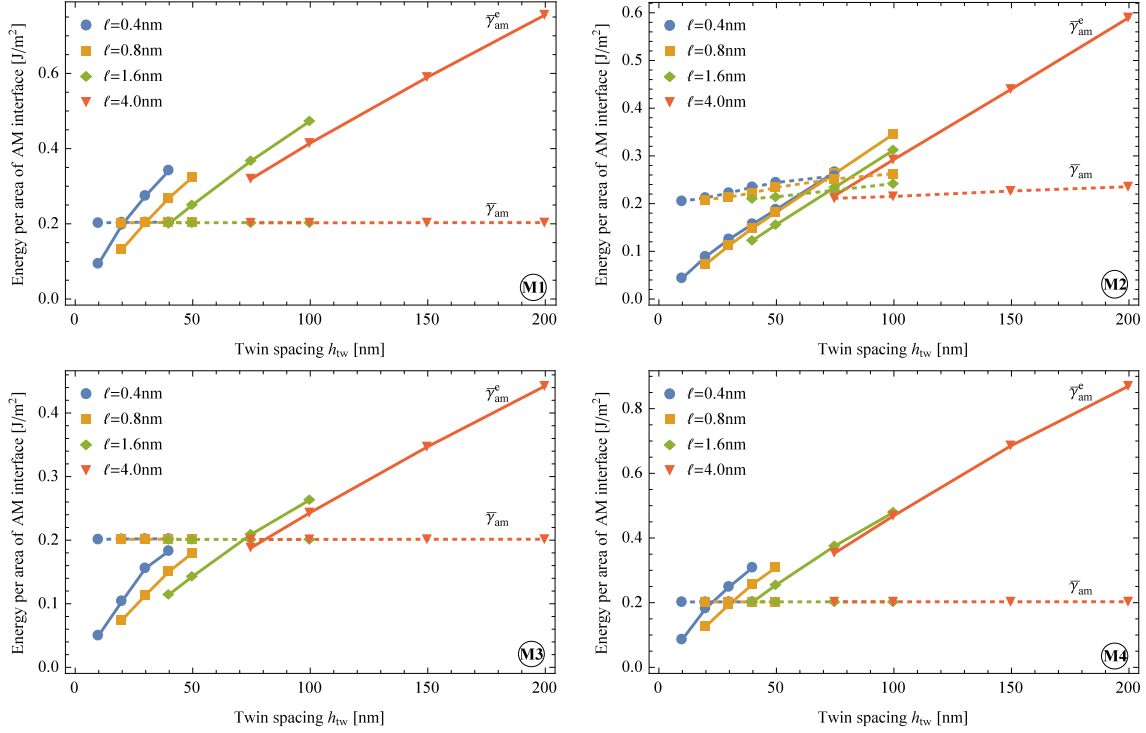


Figure 9: Dependence of the overall energy densities $\bar{\gamma}_{am}^e$ and $\bar{\gamma}_{am}$ on the twin spacing h_{tw} .

In the case of microstructures M1, M3 and M4, the overall interfacial energy density $\bar{\gamma}_{\text{am}}$ is almost constant and very close to the adopted density $\gamma_{\text{am}} = 0.2 \text{ J/m}^2$ of the interfacial energy of direct austenite–martensite interfaces. This is consistent with the results reported in Section 5.3 which indicate that the austenite–martensite interface is almost planar, thus the ratio of the actual area to the nominal one is close to 1. At the same time, the total area of zigzag-shaped interfaces in microstructure M2 exceeds the nominal area A_{R} , and thus the overall density $\bar{\gamma}_{\text{am}}$ exceeds the local density γ_{am} . Depending on h_{tw} and ℓ the corresponding factor is between 1 and 1.3.

The overall elastic micro-strain energy density $\bar{\gamma}_{\text{am}}^{\text{e}}$ increases, to the first order linearly, with increasing twin spacing h_{tw} , see Fig 9. It is thus convenient to introduce the micro-strain energy factor $\Gamma_{\text{am}}^{\text{e}}$ defined as

$$\Gamma_{\text{am}}^{\text{e}} = \frac{\bar{\gamma}_{\text{am}}^{\text{e}}}{h_{\text{tw}}}. \quad (22)$$

The dependence of $\Gamma_{\text{am}}^{\text{e}}$ on the twin spacing h_{tw} is depicted in Fig. 10. In the sharp-interface limit and for a fixed interface shape, the energy factor $\Gamma_{\text{am}}^{\text{e}}$ defined as above is size-independent (Maciejewski et al., 2005; Stupkiewicz et al., 2007). In the present phase-field modeling, $\Gamma_{\text{am}}^{\text{e}}$ does depend on the twin spacing h_{tw} because the morphology of the austenite–twinned martensite interface depends on h_{tw} as a result of complex competition between the bulk and interfacial energy contributions.

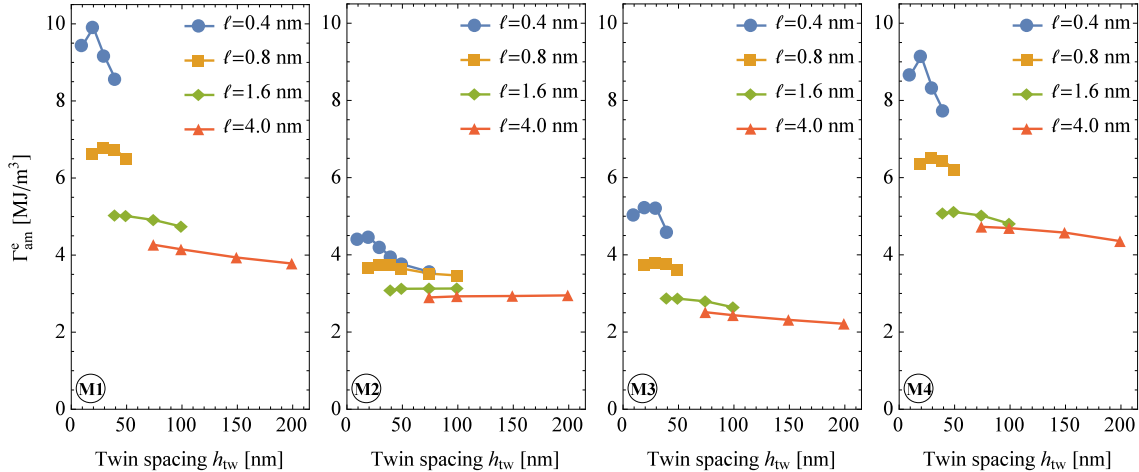


Figure 10: Dependence of the elastic micro-strain energy factor $\Gamma_{\text{am}}^{\text{e}}$ on the twin spacing h_{tw} .

It has already been discussed that the microstructures predicted by the present phase-field model depend also on the interface thickness parameter ℓ . The same applies to the individual energy contributions, in particular to the energy factor $\Gamma_{\text{am}}^{\text{e}}$. Specifically, it can be observed in Fig. 10 that $\Gamma_{\text{am}}^{\text{e}}$ increases with decreasing ℓ for a fixed twin spacing h_{tw} . This effect has already been studied by Tůma et al. (2016), where it has been shown that the corresponding dependence can be approximated by an exponential function and that the values extrapolated to $\ell \rightarrow 0$ match well the values predicted by Stupkiewicz et al. (2007) using the sharp-interface model.

Due to the reasons discussed in Section 5.1, the dependence of the energy factor Γ_{am}^e on the twin spacing h_{tw} cannot be computed at fixed ℓ for the whole range of values of h_{tw} . However, a qualitative dependence of Γ_{am}^e on h_{tw} can be deduced from the results reported in Fig. 10 and is sketched in Fig. 11. The explanation for such a dependence, referring to microstructure M2, is the following. At large twin spacing, the elastic micro-strain energy is minimized by a non-planar zigzag-shaped interface. At smaller twin spacing, the interface becomes more planar so that the total area of the austenite–martensite interface is reduced and so is the total interfacial energy. This comes at the cost of the increase in elastic strain energy contribution, as reflected by the increase of the energy factor Γ_{am}^e . However, at very small twin spacing, a decrease of the energy factor Γ_{am}^e is observed. This can be explained by noting that for a fixed interface thickness, the fraction of the volume occupied by diffuse interfaces increases with decreasing twin spacing, see the grey zones in Fig. 11. Now, highest stresses and highest densities of the elastic strain energy are expected in the vicinity of interfaces and in particular in the vicinity of triple points. However, for very small twin spacing, diffuse interfaces occupy a substantial part of the volume and thus mitigate development of high stresses. This causes reduction of the total elastic strain energy.

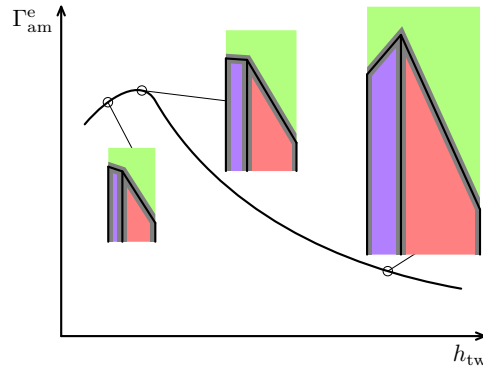


Figure 11: Scheme of the dependence of the elastic micro-strain energy factor Γ_{am}^e on the twin spacing h_{tw} at a fixed interface thickness parameter ℓ , as deduced from Fig. 10.

The above discussion applies also to microstructures M1, M3 and M4 which do not exhibit zigzag-like morphology. In that case, it is the twin branching that provides the mechanism for reduction of the elastic strain energy for increasing twin spacing. The remaining reasoning fully applies, and the dependence of Γ_{am}^e on h_{tw} is indeed qualitatively similar for all microstructures, see Fig. 10.

5.5. Interfacial energy: double-obstacle vs. double-well potential

The results reported above have been computed using the double-obstacle potential, cf. Eqs. (9) and (10). It is of interest to check whether and how the results are affected by the choice of the function that specifies the interfacial energy. Specifically, selected results have been computed using the popular double-well potential that has been used, for instance, in our previous work (Tůma et al., 2016). In case of the double-well potential, the interfacial

energy of austenite–martensite interfaces is defined as

$$F_{\Gamma}^{\text{am}} = \gamma_{\text{am}} \left(\frac{3\ell}{2} |\nabla \eta_0|^2 + \frac{6}{\ell} \eta_0^2 (1 - \eta_0)^2 \right), \quad (23)$$

where the above potential replaces that in Eq. (9), and the interfacial energy F_{Γ}^{am} of twin boundaries is redefined analogously, cf. Eq. (10).

The microstructures corresponding to the double-well potential are visibly more diffuse than those corresponding to the double-obstacle potential, see Fig. 12. Also, the zigzag angle θ is somewhat smaller in case of the double-well potential. Finally, the elastic micro-strain energy factor $\Gamma_{\text{am}}^{\text{e}}$ is smaller by 15–30% in case of the double-well potential. This effect is related to the more diffuse character of the corresponding microstructures.

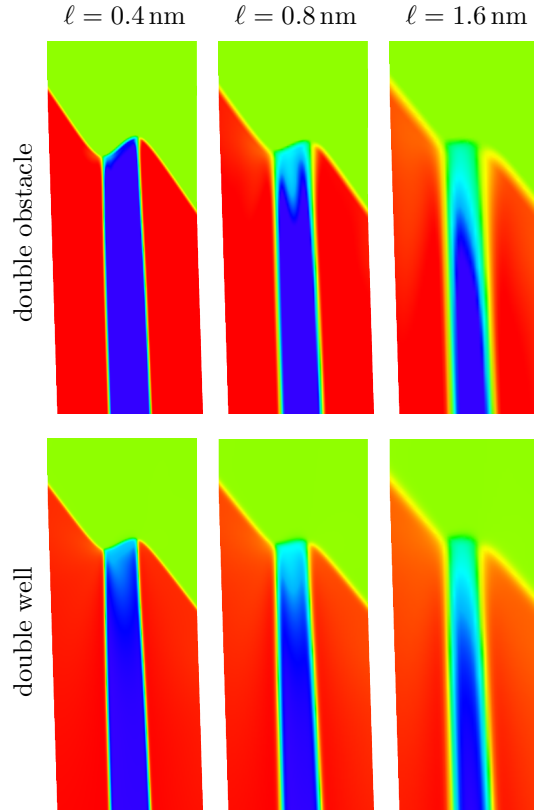


Figure 12: Comparison of the results obtained using the double-obstacle potential (upper row) and the double-well potential (lower row) for microstructure M2, $h_{\text{tw}} = 40$ nm.

5.6. Influence of interfacial energy densities γ_{tw} and γ_{am}

The interfacial energy densities γ_{tw} and γ_{am} are important material parameters that are expected to influence the results of phase-field simulations. The values of those parameters used in this work have been adopted from the literature and can only be considered as estimates of the actual values of those parameters. In this last study, the influence of parameters γ_{tw} and γ_{am} on the morphology of the austenite–martensite interface is investigated

for microstructure M3. Two values are adopted for each parameter ($\gamma_{tw} = 0.02$ or 0.04 J/m^2 , $\gamma_{am} = 0.1$ or 0.2 J/m^2), and computations are carried out for microstructure M3 using each of the corresponding four pairs of material parameters. The aim here is not to perform a complete study of the related effects, rather to illustrate selected effects and also to indicate the source of possible uncertainty in the results reported in this work.

The results are shown in Fig. 13, and two main effects can be observed. Firstly, twin branching is hindered by increasing the twin boundary energy γ_{tw} from 0.02 to 0.04 J/m^2 (the former value has been used throughout this work). This effect is naturally explained by noting that the cost of creating new interfaces is higher for higher γ_{tw} , and thus branching is not energetically favorable. Clearly, the present observation applies to the twin spacing $h_{tw} = 40 \text{ nm}$ considered here, and branching may actually occur for a larger twin spacing.

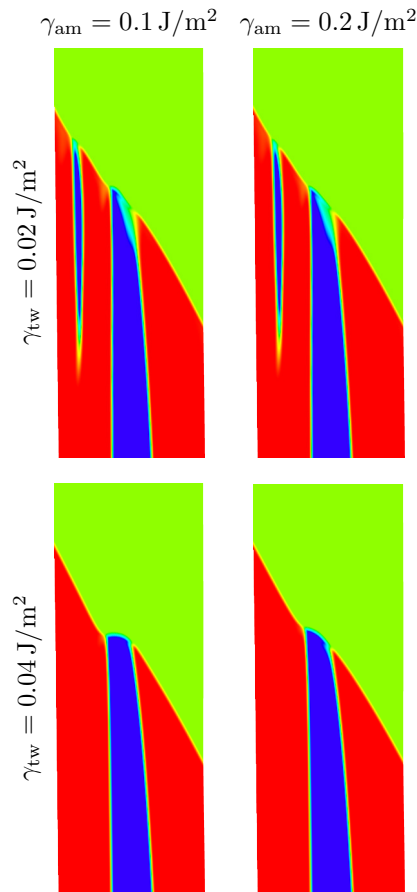


Figure 13: Influence of the interfacial energy densities γ_{tw} and γ_{am} on the resulting microstructure (microstructure M3, $h_{tw} = 40 \text{ nm}$, $\ell = 0.4 \text{ nm}$).

The second effect is related to the variation of the energy γ_{am} of austenite–martensite interfaces and is very much in line with the discussion of the zigzag-shaped interface in microstructure M2, cf. Sections 5.2 and 5.4. Specifically, the higher value of $\gamma_{am} = 0.2 \text{ J/m}^2$ (as used throughout this work) promotes a more planar austenite–martensite interface, as this reduces the related overall energy density $\bar{\gamma}_{am}$, cf. Eq. (21). This effect is clearly visible for

the non-branched zigzag-shaped interface corresponding to $\gamma_{\text{tw}} = 0.04 \text{ J/m}^2$, and it is weaker, but still visible, for the branched microstructures corresponding to $\gamma_{\text{tw}} = 0.02 \text{ J/m}^2$.

6. Conclusion

Microstructure of the austenite–twinned martensite interface in CuAlNi shape memory alloy has been simulated using the phase-field method. Twin spacing, varied between 10 and 200 nm, has been found to significantly influence the morphology of the interface layer and the energy stored in the layer. The morphology results from the competition between the elastic strain energy and the interfacial energy, the latter referring to diffuse interfaces, as implied by the phase-field method. The two energy contributions scale differently with twin spacing, and this explains the observed size effects.

At small scales, the interfacial energy dominates formation of microstructure. Accordingly, for a small twin spacing, the interface is almost planar, as this minimizes the overall interfacial energy of direct austenite–martensite interfaces. When the twin spacing is larger, the energy of elastic micro-strains, which accommodate local incompatibility of the phases, becomes more important. It is thus beneficial to reduce the elastic micro-strain energy at the cost of increased interfacial energy, and two corresponding mechanisms have been revealed. In case of one microstructure (out of four crystallographically distinct microstructures of the austenite–twinned martensite interface in CuAlNi), a zigzag-shaped interface forms, and the zigzag angle has been found to depend on the twin spacing. Here, a very good agreement has been obtained between the present phase-field simulations and the prediction of the sharp-interface model by Maciejewski et al. (2005). The remaining three microstructures exhibit a tendency to twin branching. Specifically, for larger twin spacing, the microstructure is locally refined by forming thin needle-like plates of one variant of martensite within the other one. This effectively reduces the twin spacing as well as the corresponding elastic micro-strain energy.

The phase-field simulations reported in this paper provide also an illustration of several effects related to the application of the phase-field method itself. It has been shown how the thickness of diffuse interfaces and the form of the interfacial energy influence the results. The results are also influenced by material parameters characterizing the interfacial energy of twin boundaries and direct austenite–martensite interfaces, while only rough estimates of those parameters are currently available. Finally, let us note that the present high-resolution finite-element simulations are associated with a significant computational cost, even though the problem is formulated as a two-dimensional generalized plane strain problem (in some cases, the number of unknowns exceeded 7 million). Simulation of realistic three-dimensional austenite–twinned martensite microstructures may thus be a challenging task.

Appendix A. Consistent choice of the size of the computational domain

Twin spacing h_{tw} is the main parameter that governs size-dependent microstructures at the austenite–twinned martensite interface studied in this work. However, referring to Fig. 2, the periodic unit cell depends also on plate thickness M , and that parameter may also affect the results. In particular, it has been observed that more than one period of the microstructure

may form with the computational cell if M is too small. This appendix presents a procedure for consistent determination of M for prescribed h_{tw} .

The procedure relies on the following formula that relates the twin spacing h_{tw} and the plate thickness M (Khachatryan, 1983),

$$h_{\text{tw}} = \sqrt{lM}, \quad l = \frac{\gamma_{\text{tw}}}{\Gamma_{\text{am}}^{\text{e}}}, \quad (\text{A.1})$$

where l is a characteristic length defined in terms of the twin-boundary energy γ_{tw} and the elastic micro-strain energy factor $\Gamma_{\text{am}}^{\text{e}}$, assumed here size-independent. The above formula is obtained by minimizing the total size-dependent interfacial energy of a twinned martensite plate of thickness M with respect to twin spacing h_{tw} , cf. Fig. 2. The total interfacial energy comprises two parts: the energy of twin boundaries and the energy of elastic micro-strains that accommodate local incompatibility between austenite and individual martensite variants. The former is inversely proportional to the twin spacing h_{tw} , as the density of twin boundaries (and the related energy) increases with decreasing h_{tw} . At the same time, the interfacial energy of elastic micro-strains at the austenite–twinned martensite interface is directly proportional to h_{tw} according to $\bar{\gamma}_{\text{am}}^{\text{e}} = \Gamma_{\text{am}}^{\text{e}} h_{\text{tw}}$, cf. Eq. (22). Derivation of formula (A.1) and a detailed discussion of size effects in laminated microstructures, including higher-rank laminates, can be found in Petryk et al. (2010) and Tůma et al. (2016).

Direct application of formula (A.1) to determine M for prescribed h_{tw} is not possible because the energy factor $\Gamma_{\text{am}}^{\text{e}}$, computed according to Eqs. (21) and (22), depends on h_{tw} , see Fig. 10. The plate thickness M is thus determined using the following iterative scheme. For a prescribed twin spacing h_{tw} and an initial estimate of M , the problem is solved and the energy factor $\Gamma_{\text{am}}^{\text{e}}$ is computed according to Eqs. (21) and (22). Using formula (A.1), the corresponding M is calculated and is used in the subsequent iteration. It has been checked that this iterative process is convergent. However, due to high computational cost, only three fixed-point iterations have been performed in each case.

The computational cell comprises also a layer of austenite. Its thickness (measured in the direction parallel to the twin boundary) has been chosen equal to $2h_{\text{tw}}$. It has been checked that such thickness is sufficient to ensure that two neighboring austenite–martensite interfaces do not influence each other. As a result, the total height H of the computational domain B_{C} , see Fig. 2, is $H = 2h_{\text{tw}} + M/(2 \sin \varphi)$, where $\cos \varphi = \mathbf{m} \cdot \mathbf{l}$. Thus, the prescribed control parameter $\bar{\eta}_0$, that corresponds to the average volume fraction of austenite, is equal to $\bar{\eta}_0 = 2h_{\text{tw}}/H$.

Acknowledgment. This work has been partially supported by the National Science Center (NCN) in Poland through Grant No. 2015/17/B/ST8/03242.

References

Abeyaratne, R., Chu, C., James, R. D., 1996. Kinetics of materials with wiggly energies: theory and application to the evolution of twinning microstructures in a Cu–Al–Ni shape memory alloy. *Phil. Mag. A* 73, 457–497.

- Ball, J. M., James, R. D., 1987. Fine phase mixtures as minimizers of energy. *Arch. Ration. Mech. Anal.* 100, 13–50.
- Bertsekas, D. P., 1996. *Constrained Optimization and Lagrange Multiplier Methods*, 2nd Edition. Athena Scientific, Belmont, MA.
- Bhattacharya, K., 2003. *Microstructure of martensite: why it forms and how it gives rise to the shape-memory effect*. Oxford University Press, Oxford.
- Chen, L. Q., 2002. Phase-field models for microstructure evolution. *Annu. Rev. Mater. Res.* 32, 113–140.
- Chu, C., James, R. D., 1995. Analysis of microstructures in Cu-14.0% Al-3.9% Ni by energy minimization. *J. Phys. IV* 5 (C8), 143–149.
- Clayton, J. D., Knap, J., 2011. A phase field model of deformation twinning: Nonlinear theory and numerical simulations. *Physica D* 240, 841–858.
- Finel, A., Le Bouar, Y., Gaubert, A., Salman, U., 2010. Phase field methods: Microstructures, mechanical properties and complexity. *C. R. Physique* 11, 245–256.
- Hildebrand, F. E., Miehe, C., 2012. A phase field model for the formation and evolution of martensitic laminate microstructure at finite strains. *Phil. Mag.* 92, 4250–4290.
- Hudobivnik, B., Korelc, J., 2016. Closed-form representation of matrix functions in the formulation of nonlinear material models. *Finite Elem. Anal. Design* 111, 19–32.
- Hÿtch, M. J., Vermaut, P., Malarria, J., Portier, R., 1999. Study of atomic displacement fields in shape memory alloys by high-resolution electron microscopy. *Mater. Sci. Eng. A* 273–275, 266–270.
- Khachaturyan, A. G., 1983. *Theory of Structural Transformations in Solids*. John Wiley and Sons, New York.
- Kohn, R. V., Otto, F., 1997. Small surface energy, coarse-graining, and selection of microstructure. *Physica D* 107, 272–289.
- Korelc, J., 2002. Multi-language and multi-environment generation of nonlinear finite element codes. *Engineering with Computers* 18, 312–327.
- Korelc, J., 2009. Automation of primal and sensitivity analysis of transient coupled problems. *Comp. Mech.* 44, 631–649.
- Korelc, J., Stupkiewicz, S., 2014. Closed-form matrix exponential and its application in finite-strain plasticity. *Int. J. Num. Meth. Engng.* 98, 960–987.
- Lengiewicz, J., Wichrowski, M., Stupkiewicz, S., 2014. Mixed formulation and finite element treatment of the mass-conserving cavitation model. *Tribol. Int.* 72, 143–155.

- Levitas, V. I., Levin, V. A., Zingerman, K. M., Freiman, E. I., 2009. Displacive phase transitions at large strains: phase-field theory and simulations. *Phys. Rev. Lett.* 103, 025702.
- Li, B., Luskin, M., 1999. Theory and computation for the microstructure near the interface between twinned layers and pure variant of martensite. *Mater. Sci. Eng. A* 273–275, 237–240.
- Liu, D. Z., Dunne, D., 2003. Atomic force microscope study of the interface of twinned martensite in copper-aluminium-nickel. *Scripta Mater.* 48 (12), 1611–1616.
- Maciejewski, G., Stupkiewicz, S., Petryk, H., 2005. Elastic micro-strain energy at the austenite–twinned martensite interface. *Arch. Mech.* 57, 277–297.
- Mamivand, M., Zaeem, M. A., El Kadiri, H., 2013. A review on phase field modeling of martensitic phase transformation. *Comput. Mater. Sci.* 77, 304–311.
- Mosler, J., Shchyglo, O., Hojjat, H. M., 2014. A novel homogenization method for phase field approaches based on partial rank-one relaxation. *J. Mech. Phys. Solids* 68, 251–266.
- Ostapovets, A., Zárubová, N., Paidar, V., 2012. Topological model of austenite-martensite interfaces in Cu-Al-Ni alloy. *Acta Phys. Pol. A* 122 (3), 493–496.
- Otsuka, K., Wayman, C. M. (Eds.), 1998. *Shape Memory Materials*. Cambridge University Press.
- Penrose, O., Fife, P. C., 1990. Thermodynamically consistent models of phase-field type for the kinetic of phase transitions. *Physica D* 43, 44–62.
- Petryk, H., Stupkiewicz, S., 2010. Interfacial energy and dissipation in martensitic phase transformations. Part I: Theory. *J. Mech. Phys. Solids* 58, 390–408.
- Petryk, H., Stupkiewicz, S., Maciejewski, G., 2010. Interfacial energy and dissipation in martensitic phase transformations. Part II: Size effects in pseudoelasticity. *J. Mech. Phys. Solids* 58, 373–389.
- Schryvers, D., Boullay, P., Kohn, R., Ball, J., 2001. Lattice deformations at martensite-martensite interfaces in Ni-Al. *J. Phys. IV* 11 (PR8), 23–30.
- Seiner, H., Sedlák, P., Landa, M., 2008. Shape recovery mechanism observed in single crystals of Cu–Al–Ni shape memory alloy. *Phase Trans.* 81, 537–551.
- Steinbach, I., 2009. Phase-field models in materials science. *Modelling Simul. Mater. Sci. Eng.* 17, 073001.
- Stupkiewicz, S., Maciejewski, G., Petryk, H., 2007. Low-energy morphology of the interface layer between austenite and twinned martensite. *Acta Mater.* 55, 6292–6306.
- Stupkiewicz, S., Maciejewski, G., Petryk, H., 2012. Elastic micro-strain energy of austenite-martensite interface in NiTi. *Modelling Simul. Mater. Sci. Eng.* 20, 035001.

- Stupkiewicz, S., Petryk, H., 2013. A robust model of pseudoelasticity in shape memory alloys. *Int. J. Num. Meth. Engng.* 93, 747–769.
- Suezawa, M., Sumino, K., 1976. Behaviour of elastic constants in Cu-Al-Ni alloy in the close vicinity of M_s -point. *Scripta Metall.* 10, 789–792.
- Sun, Q. P., Xu, T. T., Zhang, X., 1999. On deformation of a-m interface in single crystal shape memory alloys and some related issues. *J. Eng. Mat. Tech.* 121 (C8), 38–43.
- Tůma, K., Stupkiewicz, S., Petryk, H., 2016. Size effects in martensitic microstructures: finite-strain phase field model versus sharp-interface approach. *J. Mech. Phys. Solids*, doi: 10.1016/j.jmps.2016.04.013.
- Wang, Y., Khachaturyan, A. G., 1997. Three-dimensional field model and computer modeling of martensitic transformations. *Acta Mater.* 45, 759–773.
- Wang, Y., Li, J., 2010. Phase field modeling of defects and deformation. *Acta Mater.* 58, 1212–1235.
- Yasunaga, M., Funatsu, Y., Kojima, S., Otsuka, K., Suzuki, T., 1983. Measurement of elastic constants. *Scripta Metall.* 17, 1091–1094.
- Zárubová, N., Gemperlová, J., Gemperle, A., Dlabáček, Z., Šittner, P., Novák, V., 2010. In situ TEM observation of stress-induced martensitic transformations and twinning processes in CuAlNi single crystals. *Acta Mater.* 58 (15), 5109–5119.